Magnetically excited granular matter in low gravity

Cite as: Rev. Sci. Instrum. **90**, 054501 (2019); https://doi.org/10.1063/1.5085319
Submitted: 11 December 2018 . Accepted: 05 April 2019 . Published Online: 01 May 2019

Peidong Yu, Elmar Stärk, Guido Blochberger, Martin Kaplik, Malte Offermann, Duong Tran, Masato Adachi, and Matthias Sperl

Review of Scientific Instruments ARTICLE scitation.org/journal/rsi

Magnetically excited granular matter in low gravity

Cite as: Rev. Sci. Instrum. 90, 054501 (2019); doi: 10.1063/1.5085319
Submitted: 11 December 2018 • Accepted: 5 April 2019 •
Published Online: 1 May 2019

Peidong Yu,[a] Elmar Stärk, Guido Blochberger, Martin Kaplik, Malte Offermann, Duong Tran, Masato Adachi, and Matthias Sperl[b]

AFFILIATIONS

Institute of Materials Physics in Space, German Aerospace Center, 51147 Cologne, Germany

[a]Electronic mail: peidong.yu@dlr.de
[b]Electronic mail: matthias.sperl@dlr.de

ABSTRACT

Due to the undesired impact of gravity, experimental studies of energy-dissipative gaseous systems are difficult to carry out on ground. In the past several years, we developed a series of experimental devices suitable for various kinds of microgravity platforms. The central idea adopted in our devices is to use long-range magnetic forces to excite all the particles within the system. Through the development of our devices, different component configurations, excitation protocols, and image-capturing methods have been tried and optimized to achieve best excitation and the maximum capability for data analysis.

I. INTRODUCTION

A granular gas consists of macroscopic particles which dissipate energy when colliding with each other,[1] the manifestations of which can be found in nature, e.g., as interstellar dusts.[2] In the lab, however, to maintain the mobility of the particles, the gravity needs to be constantly countered by external excitations (e.g., Refs. 3 and 4), which preclude any continuous measurement of the overall energy dissipation, or the cooling phase, to be compared with theories.[1,5] Experiments performed in a microgravity environment in the past two decades avoided this inconvenience.[6–9] These experiments have universally used boundary shaking to excite the particles.

The kinetic theory of dissipative gaseous systems[1] assumes a homogeneous or very weakly varying spatial distribution of density and temperature of the particles. The conventional boundary shaking method does not fulfill this requirement due to the fact that the thermostat is highly favorable to those particles close to the boundary and can cause the formation of clusters in the middle.[7] In the past several years, we have adopted a different excitation method, namely, using varying magnetic field to agitate magnetic granular particles. A similar magnetic excitation method has been used in a ground experiment,[10] which requires in the first place a strong superconducting magnetic field to levitate not too many particles (~50) for excitation. We have designed a series of experimental setups for different low-gravity platforms (see Table I), where additional levitation devices are unnecessary and many more particles (>500) can be driven. The development of these setups is focused on (1) the optimization of 3D spatial and velocity distributions of the particles and (2) the accommodation of more particles and the capability of measuring them for a better statistical analysis. In this work, we will present this development of the setup and show the corresponding improvement of the resulting granular gas systems.

II. DEVELOPMENT OF THE EXPERIMENTAL SETUP

The setup can be divided into three functional parts: the sample cell, the magnetic thermostat, and the imaging system. The development of each part shall be in turn introduced in Subsections II A–II E. However, before that, we shall first provide some details of different low-gravity platforms and the properties of the sample particles.

A. Low-gravity platforms

Table II shows the basic information of all three low-gravity platforms used by our experiments.

TABLE I. A summary of the previous low-gravity campaigns.

Year	Platform	T[a] (s)	N_M[b]	N_C[c]	Particles	ϕ[d]	Results/comments
2010	Parabolic flight	22	4	1	~0.1 mm spheres, 1 × 1 mm irregular rods, and 1 × 10 mm rods	<1%	Quasi 2D excitation, no cooling, and clustering of the rods
2011	Drop tower	9.4	4	1	0.9 mm spheres and 1 × 10 mm rods	<0.4%	Quasi 2D excitation, cooling measured, and clustering of the rods
2012	Parabolic flight	22	4	2	0.06–0.9 mm spheres and 1 × 15 mm rods	<0.4%	Quasi 2D excitation, no cooling, and clustering of the rods
2015	Drop tower	9.4	8	3	0.9–2 mm spheres and 1 × 10 mm rods	<0.25%	3D excitation, cooling measured, and 3D tracking ongoing
2015	MAPHEUS	375	8	1[e]	1.6 mm spheres	~5%	3D excitation, cooling measured, and 3D tracking ongoing

[a]Duration of one continuous run of the experiment.
[b]Number of the magnets.
[c]Number of the cameras.
[d]Nominal packing fraction, only for spheres.
[e]One single light-field camera.

The parabolic flight operated by the French company Novespace provides reasonably long duration of the experiment, many chances of repetitions, and live access of the experimenters to the experiments. However, the g-jitter remains significant ($10^{-2} \sim 10^{-3} g$) and prevents any meaningful measurement of the cooling. Therefore, this platform is most suitable to test different experimental parameters or newly implemented devices.

The drop tower operated by the Center of Applied Space Technology and Microgravity (ZARM) in Bremen, Germany, offers the best low-gravity quality among the three platforms. The short duration of one experiment, however, puts an end to the cooling before its completion.

The MAPHEUS (Materials Physics Experiments under Weightlessness) is an annual sounding rocket campaign organized by the Institute of Materials Physics in Space, German Aerospace Center (DLR-MP).[11] This platform gives the longest duration of the experiment (375 s) as well as excellent remnant gravity level, meeting all low-gravity requirements of an ideal experiment. It is however a one-shot campaign and therefore becomes our ultimate experimental platform after all tests and optimizations.

B. Particles

Long range interactions between the particles in a granular gas system, within the current scope of the kinetic theory,[1] are neglected. Therefore, it is preferred that our particles are only magnetized and excited under external field $\boldsymbol{B}_0$, while they do not interact with each other due to remnant magnetization when $\boldsymbol{B}_0$ is off. In this regard, diamagnetic and paramagnetic particles should be our natural choices. The former, having been used in a previous ground experiment[10] due to their capability of being levitated, have far too weak permeability to be responsive to the mid-range external field possible to be realized on low-gravity platforms. The latter (superparamagnetic PS-based particles from microparticles GmbH), although better than the former, after being tested in our very first campaign (PFC-DLR-15), failed to yield enough dynamics within the low-gravity duration.

Eventually, we chose ferromagnetic particles provided by Sekels GmbH. The constituent material Mu-metal is a soft alloy of nickel and iron. Figure 1 shows that it offers a maximum relative permeability of $\mu_r^{max} = 4.5 \times 10^4$, guaranteeing a quick response to an external field greater than 1 mT (see Sec. II D for details)

$$F_R^{max} = \frac{\mu_0}{6}\pi R^2 M_R^2. \quad (1)$$

Equation (1) gives the estimated maximum attractive force magnitude between two touching identical spherical particles, where the maximum remnant magnetization M_R is related to the coercivity of the material H_c (see Fig. 1) as $M_R = 3H_c$, and R is the particle radius. The resulting F_R^{max} for Mu-metal particles used in our rocket campaign (see Table I) is in the order of 10^{-11} N and can thus be considered negligible (see Appendix C for detailed calculation).

TABLE II. A summary of the low-gravity platforms.

Platform	Duration (s)	Repetition per campaign	Remnant gravity (g)
Parabolic flight	22	93	$10^{-2} \sim 10^{-3}$
Drop tower	9.4	8	$\sim 10^{-6}$
MAPHEUS rocket	375	1	$\sim 10^{-5}$

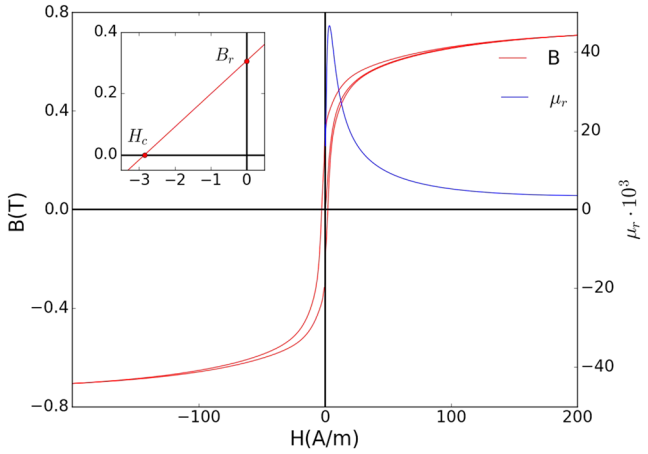

FIG. 1. The magnetization hysteresis curve and μ_r of the Mu-metal from Sekels GmbH. Inset: enlarged view in the second quadrant, showing the remanence B_r and the coercivity H_c.

C. Sample cell

The sample cell (see Fig. 2) is designed to meet several desired experimental requirements but is also under various limits demanded by different low-gravity platforms. The inner dimensions of the cell for all the campaigns are 5 × 5 × 5 cm^3, except for the rounded corners. Larger sizes will provide too much space for the external magnetic field to be effective everywhere and too much depth for the imaging system to focus on. Smaller sizes will not be enough to accommodate a necessary number of fixation holes to sustain transient hypergravity up to 50g[12] from the low-gravity platforms. The sample cell material is either polycarbonate or acrylic glass depending on different requirements of the low-gravity platforms. Both materials have negligible magnetic susceptibility ($\chi \sim 10^{-6}$, Ref. 13) and do not interfere with the magnetic field. From the very first PFC campaign, we observed attraction between the particles and the sample cell boundaries caused by static charge. In later campaigns, ESLON anti-static coating was applied to the inner side of the sample cell, removing any observable attractions.

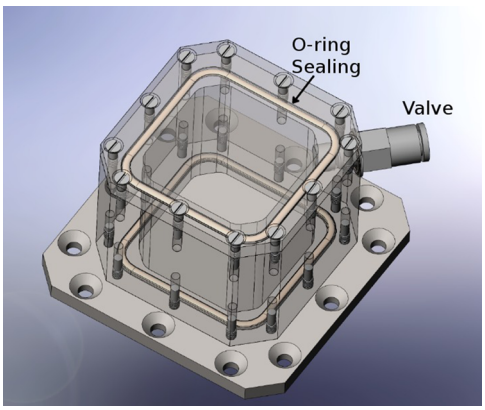

FIG. 2. The sample cell.

After fixing the top and bottom plates to the side walls of the cell, with O-rings in between to keep it air-right, the inner space of the sample cell is connected to outside only through a small electronically controlled valve. During the parabolic flight campaigns, the cell is vacuumed before the experiment with a mechanical pump, while for the drop tower and rocket campaigns, the cell is simply connected to the outer space which is already in low pressure (~10 Pa and <0.01 Pa, respectively). Then, we can estimate the air drag deceleration using the Stokes-Cunningham formula[14,15]

$$a = \frac{6\pi\eta R}{m[1 + K_n(A + B\exp(-E/K_n))]} \cdot v, \tag{2}$$

where η is the viscosity of the air, m is the particle mass, K_n is the Knudsen number calculated using the low pressure value, A, B, and E are empirically measured constants, and v is the particle velocity. The resulting prefactor of v in Eq. (2) is ~10^{-2} s^{-1} and ~10^{-4} s^{-1}. In other words, air drag reduces ~1% of the particle speed within 1 s for the parabolic flight and drop tower campaigns, while for the rocket campaign, it reduces 0.01%.

The drag deceleration in this case is only significant when, compared to particle collisions, it reduces the particle speed at about the same rate. Therefore, it is only during the cooling measurement, when particles slow down, that the results can be potentially affected. If we consider our ultimate rocket experiment (particle mean free path ~5 mm) and underestimate that each collision reduces only 1% of the speed, this scenario corresponds to a very low average particle velocity of ~0.05 mm s^{-1}. Therefore, it only affects the very late phase of the cooling measurement.

D. Magnetic excitation

We choose simple commercial holding electromagnets (GTO-80 solenoid, Mannel Magnettechnik) to excite the particles. One such electromagnet provides a spatially varying magnetic field $\boldsymbol{B}_0$. The measured inductance and resistance of one such magnet are ~4 mH and 40 Ω, respectively, resulting in a response time scale of $L/R \sim 0.1$ ms. For a soft-ferromagnetic sphere subject to an external $\boldsymbol{B}_0$ field,[16] its potential energy is

$$U = -\frac{1}{2}\boldsymbol{m} \cdot \boldsymbol{B}_0 = -\frac{3V}{2\mu_0}\left(\frac{\mu_r - 1}{\mu_r + 2}\right)B_0^2, \tag{3}$$

where V is the volume of the sphere. Given that for our Mu-metal particle material $\mu_r \gg 1$, the resulting acceleration of the sphere is simply

$$\boldsymbol{a} = \frac{3}{\mu_0\rho}(\boldsymbol{B}_0 \cdot \nabla)\boldsymbol{B}_0, \tag{4}$$

where $\rho = 8.7 \times 10^3$ kg/m^3 is the density of Mu-metal (see Appendixes A and B for detailed calculation).

For the first three campaigns in Table I, we used 4 magnets surrounding the 4 surfaces of the sample cell [see Fig. 3(a)]. The resulting minimum and maximum distance between any point inside the sample cell and the center of the magnet surface is d_{min} = 15 mm and d_{max} = 40 mm, respectively. During the last two campaigns in Table I, we increased N_C to 8 and placed them close to the 8 corners of the cubic cell with their front surfaces directed toward the center [see Fig. 3(b)]. This configuration in turn gives d_{min} = 26.7 mm and d_{max} = 70 mm. After calibrating the $\boldsymbol{B}$ field strength of our magnets

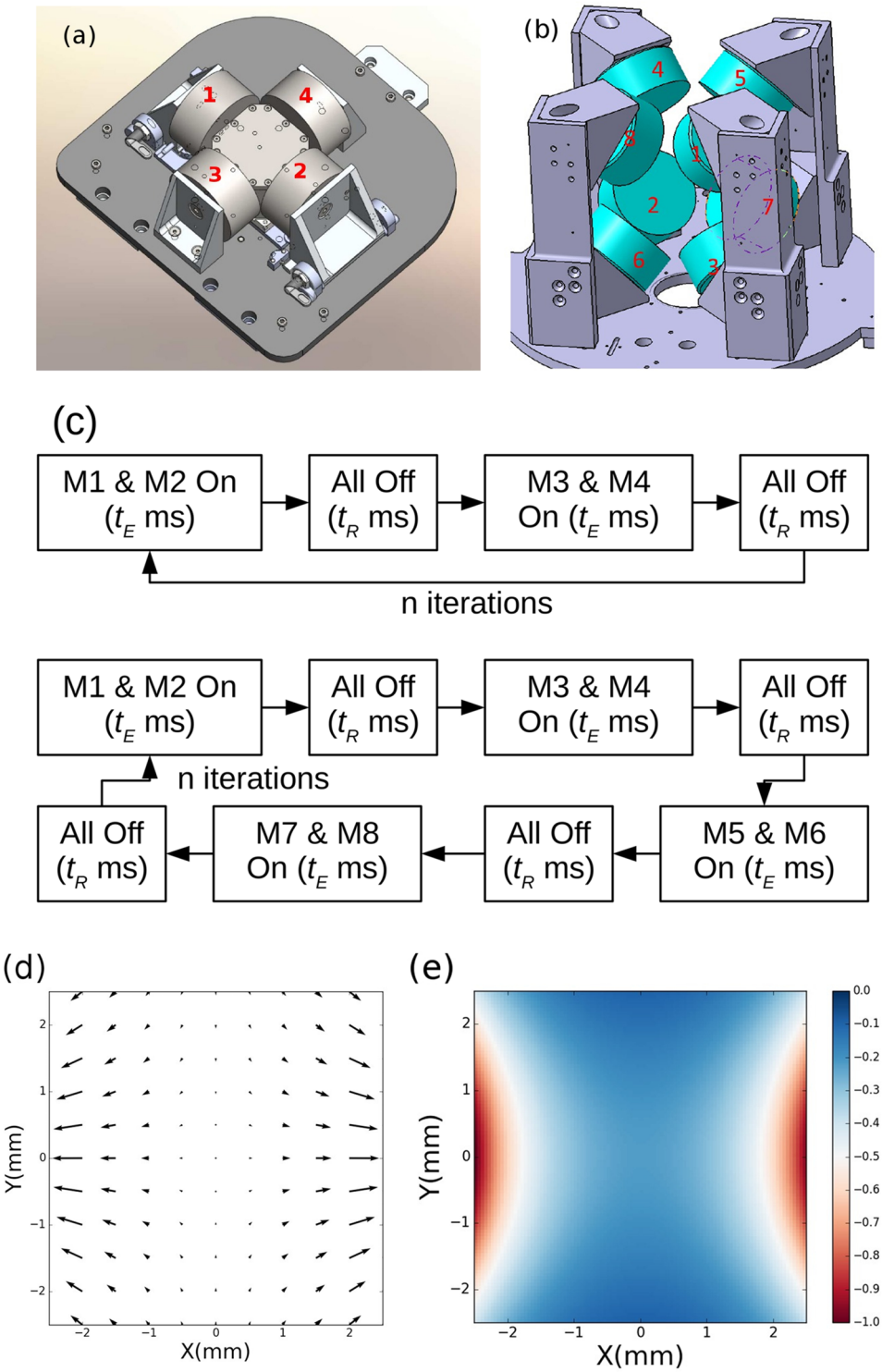

FIG. 3. (a) The 4-magnet setup, (b) the 8-magnet setup, (c) excitation sequence for the 4-magnet and 8-magnet setups, (d) simulated magnetic acceleration of one particle inside a 4-magnet setup when two opposite magnets are turned on, and (e) the potential field (normalized by maximum value) of (d).

on its symmetry axis, we are able to simulate the $\boldsymbol{B}$ field everywhere in the sample cell. Using Eqs. (3) and (4), we can then calculate the acceleration and potential of a particle at different positions, as shown in Figs. 3(d) and 3(e), from which the duration of an initially stationary particle traveling from the center to the boundary of the sample cell can be integrated. They are 0.1 s and 0.7 s for 4-magnet and 8-magnet configurations, respectively, providing us a time scale of the efficiency of the excitation.

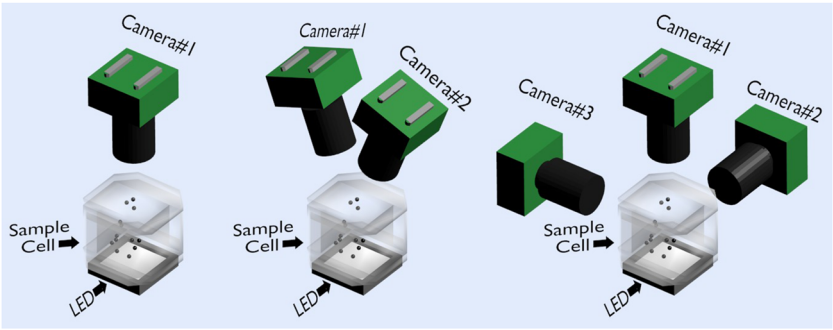

FIG. 4. Left: The one (normal or light-field) camera setup; middle: the two camera setup; and right: the three camera setup.

From the calculations above, we conclude that even at the central part of the cell, the particles experience excitations significant enough to be mobilized and the magnetic thermostat applies to the whole bulk of the cell. However, it can also be seen that unlike the previous levitated experiment[10] using diamagnetic particles, which are repelled from the boundaries, our ferromagnetic particles tend to fly toward the boundaries. In order to maintain the mobility of the particles after they collide with the boundaries, it is necessary to turn off the $\boldsymbol{B}_0$ field to allow some time for the particles to freely fly and collide with each other. Otherwise the particles would simply concentrate in the boundary regions close to the magnets. When $\boldsymbol{B}_0$ is on, it is also desired that particles be pulled symmetrically toward the boundaries to avoid concentration toward one direction that would be difficult for later excitation to alter. Therefore, at least one pair of oppositely located magnets is turned on during the excitation. Based on these criteria, as well as the calculated time scales, we tried different sequences in our parabolic flight campaign PFC-DLR-15 (see Table I). The resulting optimized sequence for a 4-magnet setup is described in Fig. 3(c), of which, (1) the magnet is either turned on at its full power or turned off completely, (2) at one time point, only two magnets facing against each other [e.g., the magnet pair labeled with 1 and 2 in Fig. 3(a)] are turned on for a time duration of t_E, while the other two are off, and (3) a relaxation phase with time duration t_R in which all magnets are off comes after (2). After numerous test runs, we found out the optimized time scales, especially for high packing fraction ϕ, to be t_E = 20 ms and t_R = 80 ms.

As for the 8-magnet setup implemented later, the only difference of the optimized sequence is that the two magnets turned on at a time are located diagonally against each other [e.g., the magnet pair labeled with 1 and 2 in Fig. 3(b)]. Therefore, when switching from pair to pair, the excitation forces applied to the particles are

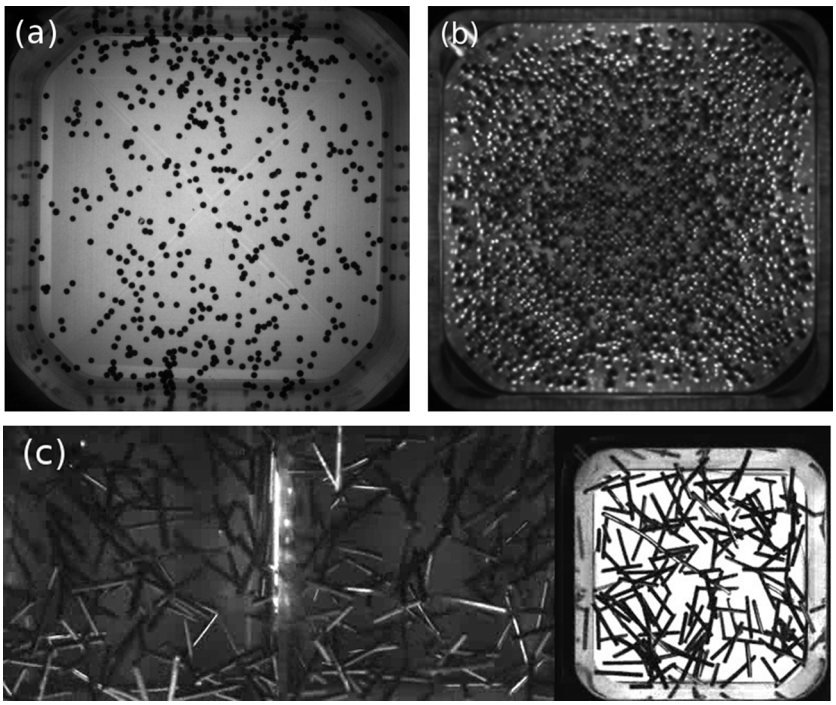

FIG. 5. Snapshots of different gas systems: (a) spherical particles with diameter 0.9 mm under the 4-magnet setup, (b) spherical particles with diameter 1.6 mm under the 8-magnet setup, and (c) cylindrical rods with diameter 1 mm and length 10 mm, under the 8-magnet setup.

in long term more isotropic in 3D space than those in the 4-magnet setup, eventually ensuring a more uniform 3D spatial distribution of the particles.

E. Imaging system

Similar to the excitation system, the imaging system of our experiment has also experienced an upgrade from 2D imaging to 3D imaging. During our first 2 campaigns with the 4-magnet system, we used only one normal high speed camera (Mikrotron EoSens mini1 or Photron FastCam MC2) to capture the motion of the particles projected onto the *xy* plane, as shown in Fig. 4.

After we had implemented the 8-magnet excitation system, it was then possible to measure the movement in the z direction as well. Two different 3D imaging methods have been adopted in our last 3 campaigns: (1) using multiple normal cameras to monitor the motions from different perspectives (Fig. 4) and (2) using one single light-field camera (Raytrix R5). For the first method, images from different cameras are analyzed using self-developed softwares based on OpenCV libraries to track the particle motion in 3D space. For the second method, we use the commercial software provided by the camera company to reconstruct the 3D depth profiles of the images, before tracking the particle positions in all dimensions.

III. RESULTING GRANULAR GASES

Using the setups and methods described in Sec. II, we have experimentally realized granular gaseous systems with different capacities and features that are ready to be explored by statistical approaches. Figure 5 shows several snapshots of these experiments.

Figure 5(a) shows our first successful experiment under the 4-magnet setup in the drop tower. Within the first half of the microgravity duration (4.7 s) offered by the facility, the setup is able to excite up to 800 spherical particles (D = 0.9 mm), corresponding to a packing fraction of ϕ = 0.0024, leaving the second half for the cooling. The setup, however, cannot completely excite all the particles within the given time, when ϕ becomes larger. Under such a low packing fraction, the particles have a relatively low chance of colliding with other particles compared with that of colliding with the sample cell boundaries. The resulting physical properties of the system are thus different from those predicted by the kinetic theory assuming the dominance of particle-particle collisions.[1]

Figures 5(b) and 5(c) show various particle systems under the 8-magnet setup. Due to the more isotropic excitation offered by more magnets, this setup is able to excite much more particles. In the ultimate sounding rocket campaign [Fig. 5(b)], the system excited ~3000 spherical particles with D = 1.6 mm within several

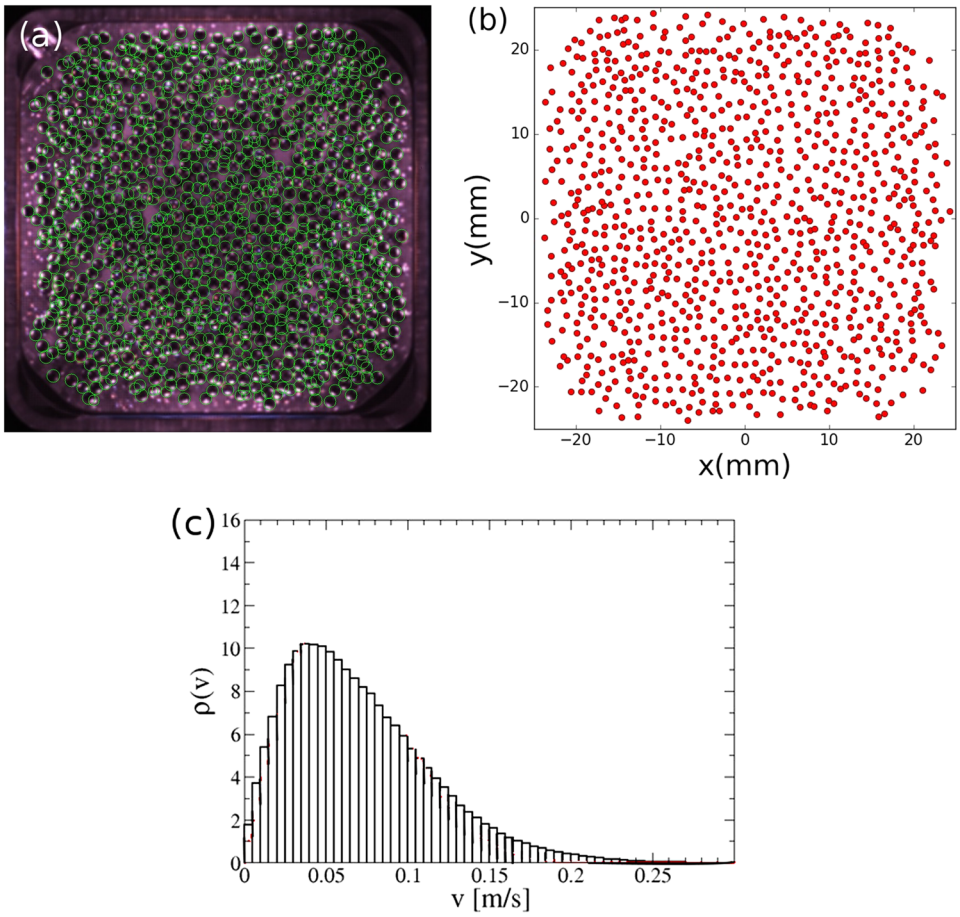

FIG. 6. (a) Snapshot of tracked particles (1.6 mm in diameter) under the 8-magnet setup, (b) spatial distribution of the particle position projected on the 2D plane, and (c) particle velocity probability density function $\rho(v)$ of the 4-magnet setup in the drop tower. Red line shows the best fit of 3D Maxwellian distribution projected onto the 2D plane.

seconds, corresponding to $\phi = 0.05$, a typical number chosen in similar experimental and simulation studies.[6,8] Figures 6(a) and 6(b) show the image processing of one snapshot from this campaign and the resulting particle position distribution projected onto the 2D plane. The homogeneity of the spatial distribution can be visually observed. The improved setup can also efficiently excite Mu-metal particles in cylindrical shape [Fig. 5(c)] which were previously very difficult to shake up by the 4-magnet setup. Figure 6(c) shows the velocity distribution measured in 2D from the drop tower experiment.

IV. CONCLUSIONS

The development of scientific experimental devices under microgravity requires many rounds of trials and errors, even when provided with maximum optimization in ground conditions. In this paper, we have shown the progress of a granular gas experimental setup developed within DLR-MP. The motivation of developing a new setup with long-range magnetic exciting force in contrast to the short-range boundary shaking force is to reach a more uniform spatial distribution of the particles. This method is further validated by our choice of the particle material: the soft ferromagnetic Mu-metal alloy that ensures quick response to the excitation field and negligible interparticle long range interactions when the field is off. Under various constraints from the available low-gravity platforms, the excitation devices and protocols have been improved from campaign to campaign to be eventually able to excite a sufficient amount of particles with different geometries within seconds in 3D space. Such devices combine into a whole experimental module with compact size and low weight that can be fitted into the most space and load-limited situation. For example, the cylindrical sounding rocket module containing the 8-magnet setup has a diameter of 438 mm, a length of 400 mm, and a weight of 40 kg (Fig. 7).

Given the capability of our setup and its adaptability to various low-gravity platforms, we consider it to be a promising candidate for future scientific experiments in the space station, where the longest low-gravity time is available for more choices of sample particles and/or more variations of excitation protocols. The availability of these variations shall provide a wide span of different relevant parameters, such as the geometry of the particles, the energy dissipation rate from the collisions, and the temperature of the gas system, for an extensive investigation of granular gas systems with uniform particle spatial distribution.

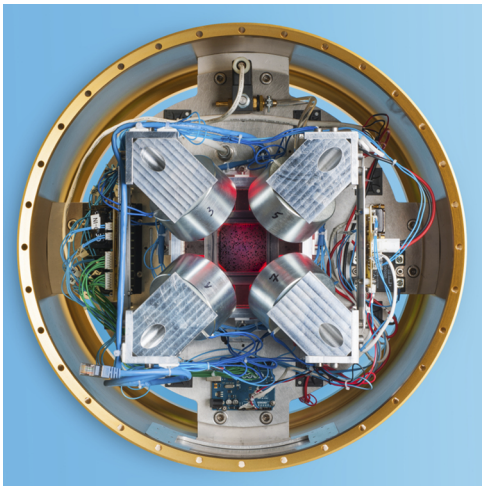

FIG. 7. Top view of the 8-magnet setup integrated into a sounding rocket module. The imaging system is not included to show the sample cell and the magnets more clearly.

ACKNOWLEDGMENTS

We appreciate the financial and administrative support from DLR, under Project Nos. 50WM1761 and 50WM1651, for the construction of the experimental setups, the data analysis, and the usage of the sounding rocket. We thank NOVESPACE and ZARM teams for providing parabolic flight and drop tower facilities for our experiments. The Japan Society for the Promotion of Science (JSPS) provides the funding (Overseas Research Fellowships) for the simulation work.

APPENDIX A: FERROMAGNETIC SPHERES IN MAGNETIC FIELD B_0

Considering a magnetized particle with magnetic moment $\boldsymbol{m}$ induced by an external magnetic field $\boldsymbol{B}_0$, its potential energy is

$$U = -\frac{1}{2}\boldsymbol{m}\cdot\boldsymbol{B}_0, \tag{A1}$$

from which the force applied to the particle can be determined as

$$\boldsymbol{F} = -\nabla U. \tag{A2}$$

The previous ground-based experimental work[10] assumes a straightforward form of $\boldsymbol{m}$ of the diamagnetic particles used in the experiment

$$\boldsymbol{m} = \frac{\mu_r - 1}{\mu_0} V\boldsymbol{B}_0, \tag{A3}$$

where V is the volume of one particle.

Equation (A3) has the merit that the relative permeability μ_r of the particle material plays a straightforward role in the prefactor, which indicates that the strength of the magnetic excitation is directly proportional to $\mu_r - 1$ (also commonly known as the susceptibility χ). In our experiments performed in low-gravity conditions, due to strict space and payload limit, it is very difficult to realize a very strong $\boldsymbol{B}_0$ field which was provided by a super-conducting magnet previously.[10] Therefore, it is tempting to choose a ferromagnetic material that has much larger μ_r than that of the diamagnetic material, the latter typically differing from 1 by only 10^{-4}.

However, Eq. (A3) is in fact a simplified version valid only for diamagnetic and paramagnetic particles with $\mu_r \sim 1$. For ferromagnetic particles with non-constant $\mu_r(H) \gg 1$, the prefactor is more complicated.[16]

The Gaussian law for magnetism dictates that

$$\nabla\cdot\boldsymbol{B} = \mu_0\nabla\cdot(\boldsymbol{H}+\boldsymbol{M}) = \mu_0(-\nabla^2\psi + \nabla\cdot\boldsymbol{M}) = 0, \tag{A4}$$

where ψ is the scalar magnetic potential defined by $\boldsymbol{H} = -\nabla\psi$. Within the sphere, we can consider the magnetization $\boldsymbol{M}$ to be uniform, which leads to $\nabla\cdot\boldsymbol{M} = 0$ and reduces Eq. (A4) to Laplace's equation

$$\nabla^2\psi = 0. \tag{A5}$$

Outside the sphere, we can safely neglect the magnetization of the very dilute remnant air in our sample cell. Equation (A5) therefore continues to hold. The general solution of Laplace's equation for spherical geometry is

$$\begin{aligned} \psi &= -C_1 r\cos\theta + \frac{C_2\cos\theta}{r^2} \quad (r > R), \\ \psi &= -C_3 r\cos\theta \quad (r \le R), \end{aligned} \tag{A6}$$

where R is the radius of the particle.

There are three boundary conditions of the problem: (1) $\boldsymbol{H}(r \to \infty) = \boldsymbol{B}_0/\mu_0$, (2) $\psi(R^+) = \psi(R^-)$, and (3) $B_r(R^+) = B_r(R^-)$, which are essentially dictated by the uniform-field assumption, the continuity of ψ, and the continuity of normal component of $\boldsymbol{B}$ at the interface, respectively. With these conditions, we can calculate C_1, C_2, and C_3 in Eq. (A6), and the full solution of ψ, which eventually leads to the $\boldsymbol{H}$ and $\boldsymbol{B}$ fields inside the sphere as

$$\begin{aligned} \boldsymbol{H} &= \left(\frac{B_0}{\mu_0} - \frac{M}{3}\right)\hat{\boldsymbol{z}} \equiv H_1\hat{\boldsymbol{z}} \quad (r \le R), \\ \boldsymbol{B} &= \left(B_0 + \frac{2\mu_0 M}{3}\right)\hat{\boldsymbol{z}} \equiv B_1\hat{\boldsymbol{z}} \quad (r \le R), \end{aligned} \tag{A7}$$

where M is the constant magnitude of the magnetization inside the square. Now these two magnitudes H_1 and B_1 are further related by the constitutive relation defined by the permeability μ_r of the particle material $B_1 = \mu_r\mu_0 H_1$. With this relation, we can derive from Eq. (A7), the final result of the total magnetic moment $\boldsymbol{m} = V\boldsymbol{M}$ as

$$\boldsymbol{m} = \frac{3(\mu_r - 1)}{\mu_r + 2} \cdot \frac{V\boldsymbol{B}_0}{\mu_0} \equiv K \cdot \frac{V\boldsymbol{B}_0}{\mu_0}, \tag{A8}$$

where $K = 3(\mu_r - 1)/(\mu_r + 2)$ is defined as the Clausius-Mossotti function.

The discrepancy between Eqs. (A3) and (A8) is apparent. For diamagnetic and paramagnetic particles with $\mu_r \sim 1$, $K \approx \mu_r - 1$ and Eq. (A3) becomes valid. For ferromagnetic particles with $\mu_r \gg 1$, $K \approx 3$ and does not depend on μ_r any more. Considering Eqs. (A1) and (A2), this conclusion indicates that, when we choose different magnetic materials for the particles with increasing μ_r, the resulting excitation force quickly saturates, and for almost all the ferromagnetic materials, the forces are the same. In other words, by choosing ferromagnetic particles instead of diamagnetic ones, we indeed are able to much more quickly excite the particles with the same $\boldsymbol{B}_0$, but not as quickly as a linear relation suggests.

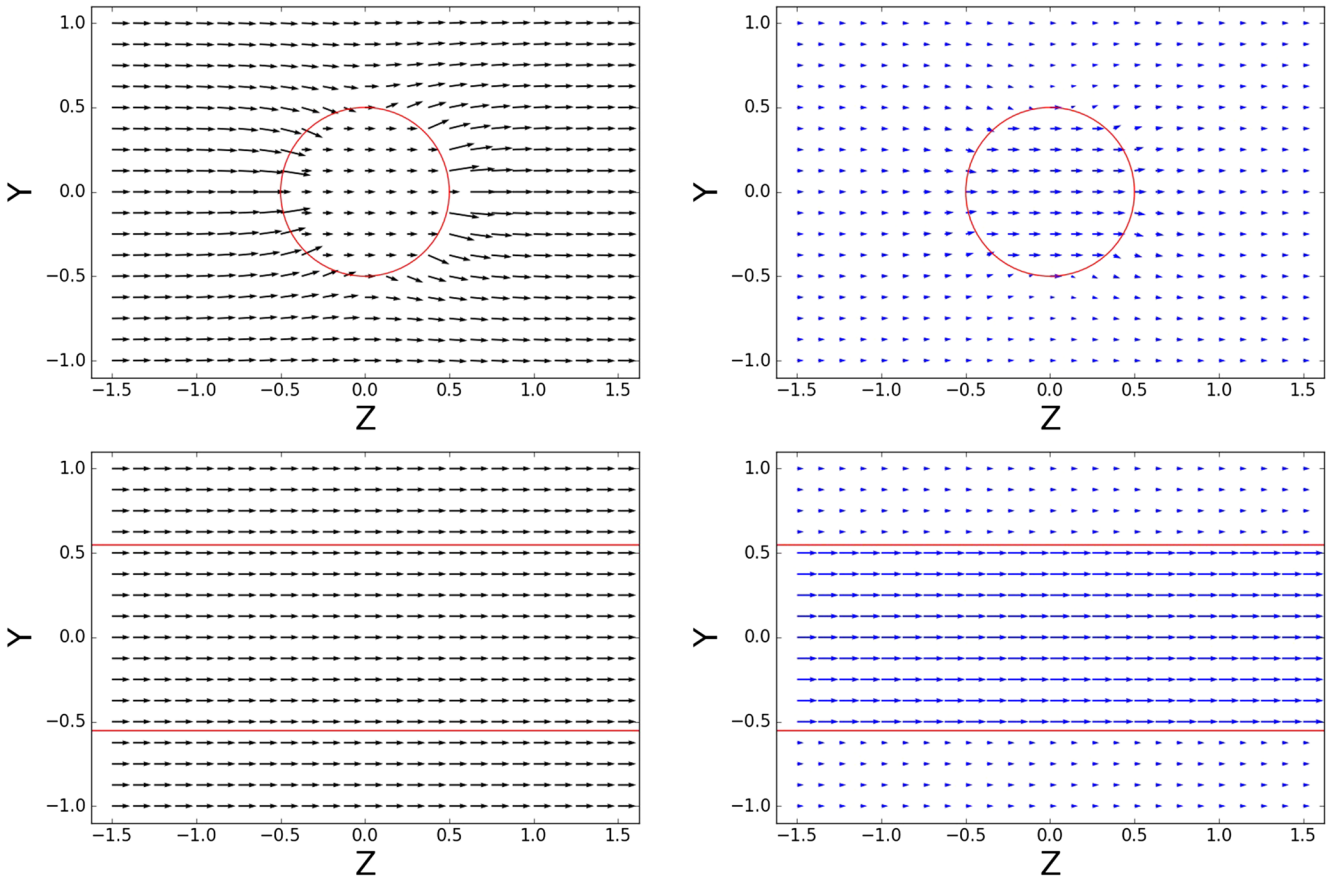

FIG. 8. The H (black) and B (blue) field of a sphere and an infinitely long rod.

Now the simple linear relation between $\boldsymbol{m}$ and μ_r in Eq. (A3) looks intuitively correct since a very straightforward understanding of the permeability μ_r is that when we place a magnetic object inside an external magnetizing field $\boldsymbol{H}_0 = \boldsymbol{B}_0/\mu_0$, the resulting magnetization $\boldsymbol{M}$ of the object should be simply $(\mu_r - 1)\boldsymbol{H}_0$. This understanding is generally wrong since the constitutive parameter μ_r only relates the local $\boldsymbol{B}$ and $\boldsymbol{H}$ fields. In other words, the $\boldsymbol{H}$ field inside the sphere is not the same as the external $\boldsymbol{H}_0$ field. From Eq. (A7), we can solve for $\boldsymbol{H}(r \le R)$,

$$H_1 = \frac{3}{\mu_r + 2} \cdot H_0 = \left(1 - \frac{1}{3}K\right) \cdot H_0 \equiv H_0 - N \cdot M. \tag{A9}$$

Again, only when $\mu_r \sim 1$, H_1 is close to H_0. In other cases, H_1 is reduced from H_0 by the additional term $KH_0/3$ or $M/3$. Effectively, this additional term partially demagnetizes the $\boldsymbol{H}$ field inside from the $\boldsymbol{H}_0$ field outside. Now a demagnetization factor N is defined here, which is 1/3 for our spherical particles. If one chooses another particle geometry, the solution to Laplace's equation (A5) with different boundary conditions can be complicated. The resulting $\boldsymbol{H}$ field inside the particle will no longer be uniform,[17] and N can become anisotropic and must be expanded into three components N_x, N_y, and N_z with $N_x + N_y + N_z = 1$.

A well-known case even simpler than the spherical geometry is an infinitely long rod with its symmetry axis placed along the $\boldsymbol{H}_0$ direction. In this case $N = 0$, $H_1 = H_0$ and $M = B_1/\mu_0 - H_1 = (\mu_r - 1)H_0$. The intuitive understanding of μ_r is now indeed correct. Therefore, for a real calibration experiment to measure μ_r (or more famously, the B-H curve) of a ferromagnetic material, a long rod is the standard sample geometry to be adopted. As shown in Fig. 8, the essential reason of this difference of N between the two geometries is that the third boundary condition, the continuity of a normal component of $\boldsymbol{B}$ at the interface, is automatically satisfied in the rod case since there is not at all any normal component of $\boldsymbol{B}$. On the other hand, in the sphere case, this continuity brings the magnetization $\boldsymbol{M}$ itself to demagnetize its own $\boldsymbol{H}$ field.

APPENDIX B: THE NONLINEAR $\mu_r(H)$ AND THE SATURATION

Unlike the paramagnetic and diamagnetic materials which can be described by one constant μ_r, the ferromagnetic materials have nonlinear $\mu_r = \mu_r(H)$ that depends on the local H field and is usually characterized by the aforementioned B-H curve. As discussed in Appendix A, as long as $\mu_r \gg 1$, the magnetic moment $\boldsymbol{m}$ does not depend on it. However, when H is large enough, the B-H curve becomes flat and the ferromagnetic material is saturated. In this case, B still increases with H, but only due to the vacuum permeability μ_0, and one should indeed be concerned about the actual μ_r value, especially because our high-permeability material usually starts to saturate at a rather low H (~200 A/m).

We take the typical maximal $B_0 = 27$ mT value of our experiment which corresponds to $H_0 = 2.1 \times 10^4$ A/m, well exceeding the saturation value. However, again because of the demagnetization effect discussed in Appendix A, the inner H_1 value is much less than H_0. After looking up the B-H curve provided by our material supplier, we estimate the inner field value to be $H_1 \approx 1.76$ A/m and the corresponding permeability $\mu_r(H = 1.76\ \text{A/m}) \approx 36\,300$. Therefore, the saturation of the material should not concern us.

Noticeably, a long rod sample particle, that can be much less demagnetized inside than a sphere, should encounter the saturation, but the demagnetization factor N also highly depends on how much the rod is aligned with $\boldsymbol{B}_0$. Considering the easily triggered rotational motion of the rods after they collide with each other, the problem becomes highly complicated and shall be explored in the future.

APPENDIX C: THE INFLUENCE OF THE REMNANT MAGNETIZATION

If we consider the case when $B_0 = 0$ and the ferromagnetic particle has some remaining magnetization M_R, Eqs. (A6)–(A8) stay valid and Eq. (A9) becomes

$$H_R = -N \cdot M_R, \tag{C1}$$

which leads to the interesting fact that inside a permanent magnet without the external field, the H field is at the opposite direction of the magnetization and thus demagnetizes the flux density field

$$B_R = \mu_0(H_R + M_R) = (1 - 1/N)\mu_0 H_R. \tag{C2}$$

In the sphere case, $N = 1/3$ and $B_R = -2\mu_0 H_R$. This linear relation defines a straight line with the negative slope in the B-H space, called the load line.

To determine the actual M_R value, one also needs the constitutive B-H curve. We assume that one of our particles is fully saturated by our $\boldsymbol{B}_0$ field. (This assumption is actually not true, as discussed in Appendix B. Therefore, the following estimate shall exaggerate the effect.) Then after turning off the $\boldsymbol{B}_0$ field, the B-H curve shall enter the second quadrant of the space, which is characterized by its intersection with the vertical axes: the remanence B_r, and its intersection with the horizontal axes: the coercivity $-H_c$. Note that the B-H curve is calibrated from a long-rod sample. These quantities should not be directly used for a magnetized sphere, whose B-H relation is further governed by the load line. The intersection of the load line and the calibrated B-H curve, called the working point, gives us the correct estimates of B_R, H_R, and M_R values, as shown in Fig. 9.

Following the procedures described above, we estimate the residual magnetization of our particles, in the fully saturated case, to

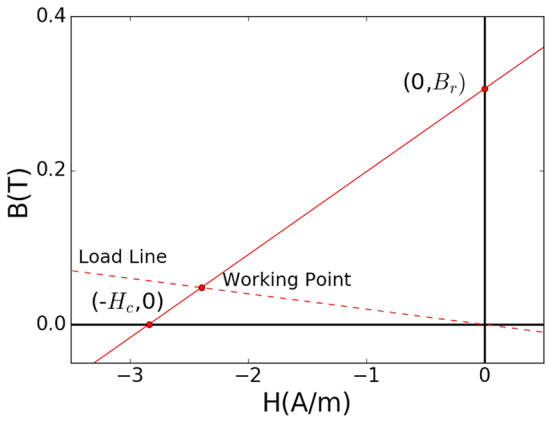

FIG. 9. The load line, the B-H curve in the second quadrant, and the working point.

be $M_R \approx 3H_c = 8.52$ A/m. (The very small slope of the load line $2\mu_0$ actually indicates that H_c is a much more useful quantity than B_r for our estimation.) If we consider two such magnetized particles of our rocket campaign (with diameter 1.6 mm) directly in contact, with their $\boldsymbol{M}_R$ parallel to each other, this situation gives us the maximal residual interaction force

$$F_R^{max} = \frac{\mu_0}{6}\pi R^2 M_R^2 = 3 \times 10^{-11} N. \quad \text{(C3)}$$

Considering the mass of one such particle (1.87×10^{-5} kg), such remnant force is negligible. If we had chosen another ferromagnetic material for our particles, e.g., annealed iron, the difference of μ_r, as discussed previously, would not make a significant difference, but the difference of H_c does. A very carefully annealed iron can still have a H_C one order of magnitude larger than that of the Mu-metal.[18] The corresponding residual force is thus 100 times larger, and the influence becomes dangerously significant.

The situation of the rods can be very different. As mentioned in Appendix B, the demagnetization factor N depends on its alignment with the $\mathbf{B_0}$ field. Because of the strong rotational motion of the rods, the problem becomes too complicated for the current work to cover and shall be investigated in the future.

REFERENCES

[1] N. Brilliantov and T. Pöschel, *Kinetic Theory of Granular Gases* (Clarendon Press, Oxford, 2003).

[2] B. T. Draine, "Interstellar dust grains," Annu. Rev. Astron. Astrophys. **41**, 241–289 (2003).

[3] J. Olafsen and J. Urbach, "Clustering, order, and collapse in a driven granular monolayer," Phys. Rev. Lett. **81**, 4369 (1998).

[4] E. Falcon, J.-C. Bacri, and C. Laroche, "Equation of state of a granular gas homogeneously driven by particle rotations," Europhys. Lett. **103**, 64004 (2013).

[5] P. K. Haff, "Grain flow as a fluid-mechanical phenomenon," J. Fluid Mech. **134**, 401–430 (1983).

[6] M. Hou, R. Liu, G. Zhai, Z. Sun, K. Lu, Y. Garrabos, and P. Evesque, "Velocity distribution of vibration-driven granular gas in Knudsen regime in microgravity," Microgravity Sci. Technol. **20**, 73 (2008).

[7] E. Falcon, R. Wunenburger, P. Evesque, S. Fauve, C. Chabot, Y. Garrabos, and D. Beysens, "Cluster formation in a granular medium fluidized by vibrations in low gravity," Phys. Rev. Lett. **83**, 440–443 (1999).

[8] E. Falcon, S. Aumaître, P. Evesque, F. Palencia, C. Lecoutre-Chabot, S. Fauve, D. Beysens, and Y. Garrabos, "Collision statistics in a dilute granular gas fluidized by vibrations in low gravity," Europhys. Lett. **74**, 830–836 (2006).

[9] A. Sack, M. Heckel, J. E. Kollmer, F. Zimber, and T. Pöschel, "Energy dissipation in driven granular matter in the absence of gravity," Phys. Rev. Lett. **111**, 018001 (2013).

[10] C. Maaß, N. Isert, G. Maret, and C. M. Aegerter, "Experimental investigation of the freely cooling granular gas," Phys. Rev. Lett. **100**, 248001 (2008).

[11] M. Siegl, F. Kargl, F. Scheuerpflug, J. Drescher, C. Neumann, M. Balter, M. Kolbe, M. Sperl, P. Yu, and A. Meyer, "Material physics rockets MAPHEUS-3/4: Flights and developments," in Proceedings of the 21st ESA Symposium on European Rocket and Balloon Programmes and Related Research, 2013.

[12] ZARM drop tower Bremen User manual, Drop Tower Operation and Service Company, 2012.

[13] M. C. Wapler, J. Leupold, I. Dragonu, D. von Elverfeld, M. Zaitsev, and U. Wallrabe, "Magnetic properties of materials for MR engineering, micro-MR and beyond," J. Magn. Reson. **242**, 233–242 (2014).

[14] M. Knudsen and S. Weber, "Luftwiderstand gegen die langsame bewegung kleiner kugeln," Ann. Phys. **341**, 981–994 (1911).

[15] Z. Li and H. Wang, "Drag force, diffusion coefficient, and electric mobility of small particles. I. Theory applicable to the free-molecule regime," Phys. Rev. E **68**, 061206 (2003).

[16] T. B. Jones, *Electromechanics of Particles* (Cambridge University Press, 2005).

[17] R. Hilzinger and W. Rodewald, *Magnetic Materials: Fundamentals, Products, Properties, Applications* (Vacuumschmelze, 2013).

[18] Kayeand Laby Online, *Tables of Physical and Chemical Constants* (National Physical Laboratory, 2005).